Modelling the black hole silhouette in Sagittarius A* with ion tori

O. Straub[1], F. H. Vincent[2,3], M. A. Abramowicz[1,4,5], E. Gourgoulhon[3], and T. Paumard[2]

[1] Nicolaus Copernicus Astronomical Center, Bartycka 18, 00-716 Warsaw, Poland
e-mail: odele@camk.edu.pl
[2] LESIA, CNRS UMR 8109, Observatoire de Paris, Université Pierre et Marie Curie, Université Paris Diderot, 92190 Meudon, France
[3] LUTH, CNRS UMR 8102, Observatoire de Paris, Université Paris Diderot, 92190 Meudon, France
[4] Department of Physics, Göteborg University, 412-96 Göteborg, Sweden
[5] Institute of Physics, Silesian University, 746-01 Opava, Czech Republic

ABSTRACT

We calculate the "observed at infinity" image and spectrum of the accretion structure in Sgr A*, by modelling it as an optically thin, constant angular momentum ion torus in hydrodynamic equilibrium. The physics we consider includes a two-temperature plasma, a toroidal magnetic field, as well as radiative cooling by bremsstrahlung, synchrotron, and inverse Compton processes. Our relativistic model has the virtue of being fully analytic and very simple, depending only on eight tunable parameters: the black hole spin and the inclination of the spin axis to our line of sight, the torus angular momentum, the polytropic index, the magnetic to total pressure ratio, the central values of density and electron temperature, and the ratio of electron to ion temperatures. The observed image and spectrum are calculated numerically using the ray-tracing code GYOTO. Our results demonstrate that the ion torus model is able to account for the main features of the accretion structure surrounding Sgr A*.

Key words. black hole physics – accretion, accretion disks – Galaxy: center
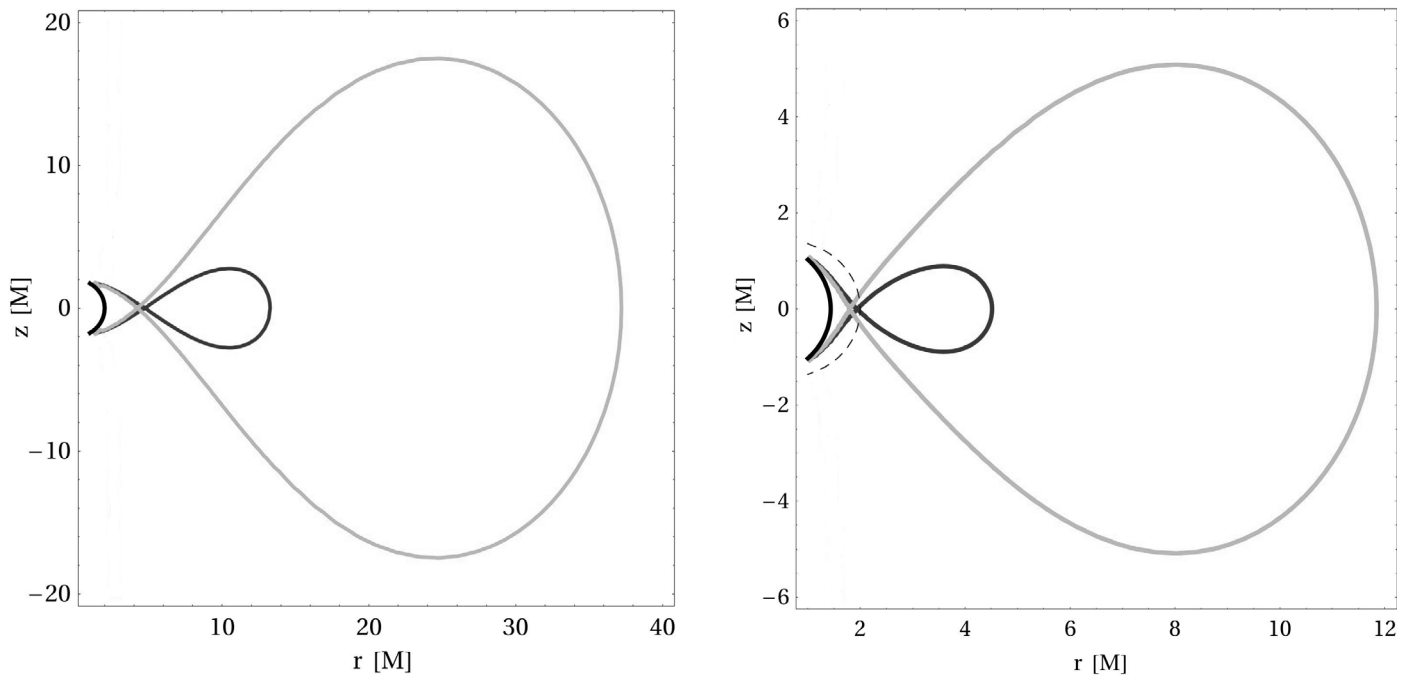
1. Introduction

The Galactic centre is one of the most interesting regions for scientific investigation because it is the closest available galactic nucleus, hence can be studied with resolutions that are impossible to achieve with other galaxies. The radio source Sagittarius A* (henceforth Sgr A*) is associated with a supermassive black hole at the centre of our Galaxy. The black hole mass, $M = 4.3 \pm 0.5 \times 10^6 \, M_\odot$, has been determined in particular from the complete and highly eccentric orbit of the star $S2$, which passes Sgr A* at its pericentre in a mere 17 light-hours, i.e. 1400 r_S, where $r_S \equiv 2GM/c^2$ is the Schwarzschild (or gravitational) radius (Schödel et al. 2002; Bower et al. 2004; Gillessen et al. 2009). Given the Sgr A* distance of 8.3 ± 0.35 kpc, the Schwarzschild radius corresponds to an angular size of around 10 μas in the sky, making the Galactic centre black hole an ideal candidate for near-future microarcsecond interferometric technologies (Paumard et al. 2008; Eisenhauer et al. 2008; Eisner et al. 2010; Broderick et al. 2011).

In this context, several authors have calculated images of various theoretical models of accretion structures around Sgr A*. Numerical simulations extend from three-dimensional non-relativistic magnetohydrodynamics (MHD, Goldston et al. 2005; Huang et al. 2007) to two-dimensional general relativistic magnetohydrodynamics (GRMHD, Mościbrodzka et al. 2009; Hilburn et al. 2010) and three-dimensional GRMHD (Dexter et al. 2010; Shcherbakov et al. 2012; Dibi et al. 2012). The size and shape of the "black hole silhouette" cast by the black hole onto the accretion structure, is determined by the photon orbit and depends only on the black hole mass and spin. Therefore, with knowledge of the black hole mass at the Galactic centre the spin can be estimated by fitting the calculated size and shape

of the shadow to the size and shape observed. The appearance (spatial extent, shape, brightness distribution, etc.) of the entire image, however, depends not only on black hole mass and spin but also on the details of the accretion structure around Sgr A*. Most of them are uncertain, e.g., the chemical abundance, the radiative processes, and the inclination. They have not yet been sufficiently examined, and a wide range of the relevant parameter space remains unexplored.

The accretion structure around Sgr A* is most probably a radiatively inefficient advection dominated accretion flow (ADAF), as Narayan et al. (1995) rather convincingly demonstrated by means of spectral fitting. In the following, an approximate analytic torus model associated with the family of Polish doughnuts introduced by Abramowicz et al. (1978) and Jaroszynski et al. (1980) is constructed for a radiatively inefficient accretion flow to describe the accretion structure in Sgr A*. The model depends on a few tunable parameters that can be changed and adjusted so that they can cover the whole parameter space of the problem. The general model of the source and the ray-tracing tailored especially for it, can be applied to spectral calculations of other black hole candidates that are both optically thin (ion tori that can be used to model e.g. some spectral states in X-ray binaries) and optically thick (Polish doughnuts, to model e.g. some luminous AGNs and ULXs).

Shapiro et al. (1976) designed a hot, two-temperature disc model to describe the strong X-ray emission observed in Cygnus X-1, which was too hot to be understood in terms of the standard model. They found an optically and geometrically thin solution branch in which ions and electrons are weakly coupled, having different temperatures and being in energy balance. This solution, however, is thermally unstable.

Fig. 1. Meridional cut through a $\lambda = 0.3$ (black curve) and a $\lambda = 0.7$ torus (grey curve) around a black hole (the black semi-circle is the event horizon). *Left panel:* Schwarzschild case. *Right panel:* Kerr case with $a = 0.9\,M$, the long-dashed semi-circle marking the ergosphere.

Ion tori were proposed independently by Ichimaru (1977) (though using different terminology) and Rees et al. (1982) to model a gas flow that emits little detectable radiation but is at the same time able to power radio jets, both in galactic sources and microquasars. Ion tori are geometrically thick, gas (ion) pressure-supported spheroidal structures, located in the inner regions of accretion flows. They are extremely optically thin and very radiatively inefficient. These ion tori consist of a fully ionised plasma, hence their name, in which protons and electrons are thermally decoupled (each following its own temperature distribution) and not in local energy balance. They are assumed to be low-α accretion flows threaded with magnetic fields, so that the ordinary molecular viscosity is suppressed in favour of magnetic/turbulent viscosity[1]. Owing to their vertically extended shape, $H/r \lesssim 1$, ion tori naturally create a pair of funnels through which magnetic flux can collimate and escape. Ion tori only exist in the sub-Eddington accretion regime, $\dot{M} < \dot{M}_{\rm crit} < \dot{M}_{\rm Edd}$ (see e.g. Ichimaru 1977; Rees et al. 1982), where radiative cooling is inefficient enough for ions to remain sufficiently hot (near virial) during the whole inflow time, i.e., $t_{\rm diff} \gg t_{\rm accr}$. Otherwise, at higher mass-accretion rates, cooling causes the puffed-up inner spheroidal region to gradually become opaque and deflate to a standard thin disc. As a consequence of $t_{\rm diff} \gg t_{\rm accr}$, the ions carry most of the energy with them into the black hole. Instead of "the ions are not cooling down fast enough", one may also and equivalently say that the disc is locally "advectively cooled" because energy is carried away by ions. Therefore, this branch of solutions was renamed to "advection dominated accretion flow" (ADAF, see e.g. Narayan & Yi 1994, 1995; Abramowicz et al. 1995; Esin et al. 1997).

In this work, we model Sgr A* by ion tori very much similar to these described by Rees et al. (1982). They are based on the mathematical description introduced by Paczyński and collaborators in their studies of *Polish doughnuts*

Abramowicz et al. 1978; Jaroszynski et al. 1980. Although Polish doughnuts share some of their important characteristics that are completely the *opposite* of these of ion tori (they are optically thick, radiation pressure supported, and correspond to super-Eddington accretion rates, $\dot{M} \gg \dot{M}_{\rm Edd}$), both classes of tori have the same equipotential structure and very similar dynamical properties. In particular, they both have a "Roche lobe", i.e. a critical equipotential that crosses itself along the "cusp" at $r = r_{\rm cusp}$ (see Fig. 1). Roche lobe overflow causes *dynamical* mass loss from the torus to the black hole, with no need of help from viscosity. Thus, the accretion flow at radii $r \le r_{\rm cusp}$ is regulated by the black hole strong gravity and not by viscous processes. The cusp should be regarded as the *inner edge of the disc*; for low accretion rates it corresponds to ISCO, whereas for higher accretion rates the cusp is closer to the black hole. Both ion tori and Polish doughnuts are dynamically unstable in terms of the Papaloizou & Pringle (1984) instability. However, as proven by Blaes (1987), this instability is suppressed by the Roche lobe overflow (see also Narayan & Popham 1993).

These properties, which are shared by ion tori and Polish doughnuts, are also genuine and robust for much more general toroidal structures around black holes. In particular, they do not depend on the angular momentum distribution inside the torus. It is customary to assume that angular momentum is constant, $\ell = \ell_0 = {\rm const.}$, as this leads to *remarkably simple* final analytic formulae. This is an assumption adopted here. With this, we do not pretend to provide a realistic accretion scenario, but an easily accessible yet powerful analytical analogy. In follow-up papers, we will relax this assumption and calculate the observed properties of ion tori with $\ell \neq {\rm const.}$ Dynamical models for these tori have been calculated e.g. by Qian et al. (2009).

The paper is structured as follows. In Sect. 2, we construct the hydrodynamical torus and in Sects. 3 and 4 we discuss the radiative properties. Section 5 shows the resulting spectra in relation to broadband data of Sgr A* and a series of images. The presented spectra are neither chi-squared fits nor best guesses,

---

[1] The α-prescription is also applied in this context.

they merely illustrate the performance of the ion torus model. Section 6 presents the conclusions.

2. The geometry of fat tori

2.1. Kerr metric

In Boyer-Lindquist spherical coordinates (t, r, θ, ϕ), geometrical units $c = 1 = G$, and signature $(-, +, +, +)$, the Kerr metric line element has the form

$$
\mathrm{d}s^2 = -\left(1 - \frac{2Mr}{\Xi}\right)\mathrm{d}t^2 - \frac{4Mra}{\Xi}\sin^2\theta\,\mathrm{d}t\,\mathrm{d}\phi + \frac{\Xi}{\Delta}\,\mathrm{d}r^2
$$
$$
+ \Xi\,\mathrm{d}\theta^2 + \left(r^2 + a^2 + \frac{2Mra^2\sin^2\theta}{\Xi}\right)\sin^2\theta\,\mathrm{d}\phi^2, \tag{1}
$$

where M is the black hole mass, $a \equiv J/M$ its reduced angular momentum (J being the black hole angular momentum), $\Xi \equiv r^2 + a^2\cos^2\theta$, and $\Delta \equiv r^2 - 2Mr + a^2$.

Circular orbits in Kerr spacetime are obtained from the time-like geodesics of the metric in Eq. (1) for which the four-velocity takes the form $u^\mu = (u^t, 0, 0, u^\phi)$. The two constants of geodesic motion, which are associated respectively with stationarity and axisymmetry, are then expressible as

$$
\mathcal{E} = -u_t = -u^t\,(g_{tt} + \Omega\,g_{t\phi}), \tag{2}
$$
$$
\mathcal{L} = u_\phi = u^t\,(g_{t\phi} + \Omega\,g_{\phi\phi}), \tag{3}
$$

where

$$
\Omega \equiv \frac{u^\phi}{u^t} \tag{4}
$$

is the angular velocity with respect to a distant observer. The specific angular momentum is defined by

$$
\ell \equiv \frac{\mathcal{L}}{\mathcal{E}} = -\frac{u_\phi}{u_t}. \tag{5}
$$

At circular *geodesic* orbits, the angular momentum has its "Keplerian" form (Bardeen et al. 1972):

$$
\ell_K(r, a) = \frac{M^{1/2}\left(r^2 - 2aM^{1/2}r^{1/2} + a^2\right)}{r^{3/2} - 2Mr^{1/2} + aM^{1/2}}. \tag{6}
$$

Here and in the remainder of the article, we consider M as a fixed parameter, so that we can assume ℓ_K to be a function only of (r, a).

Important circular orbits in the Kerr metric are the marginally stable and marginally bound ones, corresponding to values of r (Bardeen et al. 1972)

$$
r_{ms}(a) = M\left[3 + z_2 - ((3 - z_1)(3 + z_1 + 2z_2))^{1/2}\right], \tag{7}
$$
$$
r_{mb}(a) = 2M - a + 2M^{1/2}(M - a)^{1/2}, \tag{8}
$$

where $z_1 \equiv 1 + (1 - a^2/M^2)^{1/3}\left[(1 + a/M)^{1/3} + (1 - a/M)^{1/3}\right]$ and $z_2 \equiv (3a^2/M^2 + z_1^2)^{1/2}$. On these special orbits, the specific angular momentum takes the values

$$
\ell_{ms}(a) = \ell_K(r_{ms}(a), a) \quad \text{and} \quad \ell_{mb}(a) = \ell_K(r_{mb}(a), a). \tag{9}
$$

2.2. Fluid torus of constant specific angular momentum

We consider a fluid torus of negligible self-gravitation around a Kerr black hole. Modelling the fluid as a perfect one, the stress-energy tensor is

$$
T_{\mu\nu} = (\epsilon + P)\,u_\mu u_\nu + Pg_{\mu\nu}, \tag{10}
$$

where P is the fluid pressure and ϵ the fluid proper energy density. For a purely circular motion ($u^\mu = u^t(1, 0, 0, \Omega)$), it can be shown that the energy-momentum conservation equation, $\nabla_\nu T^\nu{}_\mu = 0$, takes the form

$$
\frac{\nabla_\mu P}{\epsilon + P} = -\nabla_\mu \ln(-u_t) + \frac{\Omega\nabla_\mu \ell}{1 - \Omega\ell}, \tag{11}
$$

with ℓ related to the fluid four-velocity components by Eq. (5). Assuming that the fluid is barotropic, $P = P(\epsilon)$, we introduce the enthalpy function

$$
H \equiv \int_0^P \frac{\mathrm{d}P}{\epsilon + P}, \tag{12}
$$

so that the left-hand side of Eq. (11) becomes simply $\nabla_\mu H$. Following Abramowicz et al. (1978), we consider models for which ℓ is constant within the entire torus (see also Sect. 1):

$$
\ell = \ell_0. \tag{13}
$$

Accordingly, the equation of motion in Eq. (11) reduces to $\nabla_\mu H = -\nabla_\mu \ln(-u_t)$ yielding

$$
H = W + \text{const.}, \tag{14}
$$

where we have introduced the potential

$$
W \equiv -\ln(-u_t). \tag{15}
$$

From the normalisation relation $u_\mu u^\mu = -1$, we get

$$
W(r, \theta) = \frac{1}{2}\ln\left[-\frac{g_{tt} + 2\Omega g_{t\phi} + \Omega^2 g_{\phi\phi}}{(g_{tt} + \Omega g_{t\phi})^2}\right], \tag{16}
$$

where Ω should be considered as the function of (r, θ)

$$
\Omega(r, \theta) = -\frac{g_{t\phi} + \ell_0 g_{tt}}{g_{\phi\phi} + \ell_0 g_{t\phi}}. \tag{17}
$$

This last relation is easily derived by combining Eqs. (2), (3) and (5).

Abramowicz et al. (1978) proved that the cusp location should be between the marginaly stable and the marginaly bound orbit, which implies that ℓ_0 must obey

$$
\ell_{ms}(a) < \ell_0 < \ell_{mb}(a), \tag{18}
$$

with $\ell_{ms}(a)$ and $\ell_{mb}(a)$ given by Eq. (9). Recast in terms of the dimensionless parameter

$$
\lambda \equiv \frac{\ell_0 - \ell_{ms}(a)}{\ell_{mb}(a) - \ell_{ms}(a)}, \tag{19}
$$

the condition in Eq. (18) is equivalent to

$$
0 \leq \lambda \leq 1. \tag{20}
$$

Given the radial dependence in Eq. (6) of the Keplerian specific angular momentum, which takes its minimum at $r = r_{ms}(a)$, and

the constraint of Eq. (18), there are two values of r, r_{in}, and r_c say, for which $\ell_K(r, a) = \ell_0$. One has necessarily

$$r_{mb}(a) < r_{in} < r_{ms}(a) < r_c. \tag{21}$$

Since for $r = r_{in}$ or $r = r_c$, the actual angular momentum ℓ_0 is equal to the Keplerian one, the gravity and centrifugal forces balance each other, implying that $\nabla_\mu W = 0$. From the first integral in Eq. (14), we then have $\nabla_\mu H = 0$, or equivalently, via Eq. (12), $\nabla_\mu P = 0$. A point where the gradient vanishes can be called either a singular point (self-crossing of an equipotential) or an extremum. In the present case, $r = r_{in}$ is the location where one of the equipotentials of W, the so-called *Roche lobe*, self-crosses, as shown in Fig. 1. This gives rise to a cusp at the torus surface (Abramowicz et al. 1978). On the other side, $r = r_c$ corresponds to the maximum of P. The circle $r = r_c$ in the equatorial plane is called the *centre* of the torus.

2.3. Torus solution for a polytropic equation of state

To go further, we assume a polytropic equation of state

$$P = K\epsilon^{1+1/n}, \tag{22}$$

where K and n are two constants, n being the *polytropic index* and K the *polytropic constant*. The total energy density $\epsilon = \rho + \Pi$ is the sum of energy density ρ and internal energy Π, which in the non-relativistic limit, $\Pi \ll \rho$, reduces to $\epsilon \simeq \rho$. Equation (12) is then readily integrated, yielding

$$H = (n + 1) \ln \left(1 + K\epsilon^{1/n}\right). \tag{23}$$

The surface of the torus is defined by $P = 0$. From Eq. (22), this corresponds to $\epsilon = 0$, and from Eq. (23) to $H = 0$. Therefore, we may rewrite the first integral of motion in Eq. (14) as

$$H = W - W_s, \tag{24}$$

where the constant W_s is the value of the potential W at the torus surface. Denoting by H_c and W_c the values of H and W at the torus centre, Eq. (24) implies that

$$H_c = W_c - W_s. \tag{25}$$

We introduce the dimensionless potential

$$\omega(r, \theta) \equiv \frac{W(r, \theta) - W_s}{W_c - W_s}. \tag{26}$$

From Eqs. (24) and (25), we have

$$H = H_c \omega. \tag{27}$$

Substituting Eq. (23) for H, we get

$$\ln \left(1 + K\epsilon^{1/n}\right) = \omega \ln \left(1 + K\epsilon_c^{1/n}\right),$$

where ϵ_c is the energy density at the torus centre. Solving for ϵ, we obtain

$$\epsilon = \frac{1}{K^n} \left[(K\epsilon_c^{1/n} + 1)^\omega - 1\right]^n. \tag{28}$$

At this stage, our torus model is determined by five parameters (in addition to the black hole mass M): the Kerr spin parameter a, the dimensionless specific angular momentum λ, the polytropic index n, the polytropic constant K, and the central density ϵ_c. From λ and a, we evaluate ℓ_0 via Eq. (19). The values of ℓ_0 and a fully determine the potential $W(r, \theta)$ according to Eqs. (16), (17).

Since we are seeking a Roche-lobe filling torus, the value W_s of the potential W at the torus surface must be set to the value at the Roche lobe (cf. Sect. 2.2)

$$W_s = W(r_{in}, \pi/2). \tag{29}$$

Given W_s and H_c (deduced from ϵ_c in Eq. (23)), we determine W_c using Eq. (25). We know then entirely the dimensionless potential $\omega(r, \theta)$ as given by Eq. (26). We can thus compute the energy density everywhere in the torus using Eq. (28).

We note that, by construction (cf. Eq. (26)), ω is zero at the surface of the torus and one at the centre. Between $0 \leq \omega(r, \theta) \leq 1$, the toroidal equipotentials extend from the largest possible area, the torus surface, down to a single line, a circle at r_c. Open equipotential surfaces have $\omega(r, \theta) < 0$. The size of the Roche lobe tori depends on the spin. The higher the spin, the narrower the angular momentum distribution that sets the location of the critical radii, hence the smaller the tori. For a fixed value of a, the Roche torus is the largest, having an infinite outer radius r_{out}, when $\lambda = 1$, i.e., $\ell_0 = \ell_{mb}(a)$.

3. Adding physics

In what follows, we set $n = 3/2$, which corresponds to the adiabatic index $\gamma = 1 + 1/n = 5/3$ of a non-relativistic ideal gas with no radiation pressure. This is consistent with the existence of a very optically thin medium.

3.1. Thermodynamic quantities

In optically thin gas-pressure-supported ion tori, the radiation pressure can be neglected. The total pressure P is expressed as the sum of the magnetic and gas contributions, P_{mag} and P_{gas}

$$P = P_{mag} + P_{gas}. \tag{30}$$

The magnetic and gas pressures are assumed to be some fixed parts of the total pressure (an assumption that is often made in analytic models of accretion structures)

$$P_{mag} = \frac{B^2}{24\pi} = \beta P, \qquad P_{gas} = (1 - \beta) P, \tag{31}$$

were B is the intensity of magnetic field. The gas is assumed to be a two-temperature plasma, with μ_i, μ_e, T_i, and T_e being the mean molecular weights and temperatures of ions and electrons, respectively. The gas pressure is then expressed as the sum of the ion and electron contributions

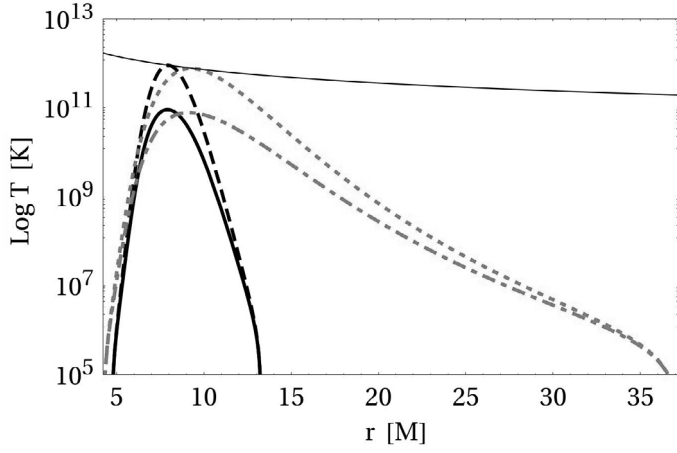$$P_{gas} = P_i + P_e = \frac{k_B}{m_u} \epsilon \left(\frac{T_i}{\mu_i} + \frac{T_e}{\mu_e}\right), \tag{32}$$

where k_B is the Boltzmann constant and m_u is the atomic mass unit. We write the ion and electron temperatures as

$$T_e = f(\omega)\mu_e \frac{m_u P_{gas}}{k_B \epsilon}, \qquad T_i = g(\omega)\mu_i \frac{m_u P_{gas}}{k_B \epsilon}, \tag{33}$$

where f and g are linear functions of the equipotential function ω.

We note that the model does not consider heating and cooling of the accretion structure, but assumes thermal equilibrium with a given temperature distribution. While this may not represent the real situation, it is still an adequate approximation supported by MHD simulations that self-consistently include cooling and

Fig. 2. Ion (dashed/dotted) and electron (solid/dot-dashed) temperature distribution throughout a $\lambda = 0.3$ torus (black) and a $\lambda = 0.7$ torus (grey) around a Schwarzschild black hole. We assume a central ion to electron temperature ratio of $\xi = 0.1$. The thin black line marks $T_{\rm vir}$.

heating in the dynamics. Dibi et al. (2012) found that these processes are *not* dynamically important in the parameter range corresponding to Sgr A*. We assume here that the ion and electron temperatures are equal at the surface: $T_{\rm i} = T_{\rm e}$ when $\omega = 0$, and that they are at some particular ratio ξ at the centre $\xi T_{\rm i} = T_{\rm e}$ when $\omega = 1$. This leads to

$$f(0) = \frac{\mu_{\rm i}}{\mu_{\rm e} + \mu_{\rm i}} \equiv \mathcal{M}, \tag{34}$$

$$f(1) = \frac{\mu_{\rm i}\xi}{\mu_{\rm e} + \mu_{\rm i}\xi} \equiv \mathcal{M}_\xi, \tag{35}$$

and since Eq. (32) is fulfilled when $f(\omega) + g(\omega) = 1$, one easily finds values of $g(0)$ and $g(1)$ that allow us to write explicit expressions for the two temperatures

$$T_{\rm e} = \left[(1 - \omega)\mathcal{M} + \omega\mathcal{M}_\xi\right]\mu_{\rm e}\frac{(1 - \beta)m_{\rm u}P}{k_{\rm B}\epsilon}, \tag{36}$$

$$T_{\rm i} = \left[\frac{\mu_{\rm e}}{\mu_{\rm i}}\mathcal{M} + \omega(\mathcal{M} - \mathcal{M}_\xi)\right]\mu_{\rm i}\frac{(1 - \beta)m_{\rm u}P}{k_{\rm B}\epsilon}. \tag{37}$$

It is often practical to express equations in terms of the dimensionless temperatures

$$\theta_{\rm e} = \frac{k_{\rm B}T_{\rm e}}{m_{\rm e}c^2}, \quad \text{and} \quad \theta_{\rm i} = \frac{k_{\rm B}T_{\rm i}}{m_{\rm i}c^2}, \tag{38}$$

were $m_{\rm e}$ and $m_{\rm i}$ are the electron and ion masses.

Figure 2 shows the temperature distribution in tori. It is different from the ADAF self-similar solution (e.g., Narayan & Yi 1995), which *being self-similar* must be a monotonic function of radius. Here, the non-monotonicity of the temperature curves has its roots in the existence of *boundaries*, the outer occurring at the outer torus radius and the inner at the cusp. The ion and electron temperatures have a maximal separation (given by ξ) at the torus centre and converge towards either end of the torus. The temperature in our model is obviously zero at these boundaries. We note that in the torus interior our curves and those of Narayan & Yi (1995) are clearly consistent. Using Eq. (32), one can now derive the relation for the polytropic constant at the torus centre

$$K = \frac{kT_{\rm e,c}}{(1 - \beta)m_{\rm u}\epsilon_{\rm c}^{2/3}\mu_{\rm e}\mathcal{M}_\xi}, \tag{39}$$

where $T_{\rm e,c}$ is the central electron temperature. The total pressure is

$$P = \frac{k_{\rm B}T_{\rm e,c}}{(1 - \beta)\mu_{\rm e}m_{\rm u}\mathcal{M}_\xi}\frac{\epsilon^{5/3}}{\epsilon_{\rm c}^{2/3}}, \tag{40}$$

and the magnetic field

$$B = \left[\frac{24\pi\beta}{(1 - \beta)}\frac{k_{\rm B}T_{\rm e,c}}{\mu_{\rm e}m_{\rm u}\mathcal{M}_\xi}\frac{\epsilon^{5/3}}{\epsilon_{\rm c}^{2/3}}\right]^{1/2}. \tag{41}$$

The thermodynamic relations between T, P, and ϵ require the knowledge of the mean molecular weight μ, which is linked to the ion and electron molecular weights by

$$\mu = \left[\frac{1}{\mu_{\rm i}} + \frac{1}{\mu_{\rm e}}\right]^{-1} \approx \frac{2}{1 + 3X + Y/2} \tag{42}$$

with

$$\mu_{\rm i} = \frac{\epsilon}{n_{\rm i}m_{\rm u}} = \frac{4}{4X + Y} \quad \text{and} \quad \mu_{\rm e} = \frac{\epsilon}{n_{\rm e}m_{\rm u}} = \frac{2}{1 + Y}, \tag{43}$$

where X and Y are the hydrogen and helium abundances, which are assumed to be equal to $X = 0.75$ and $Y = 0.25$ as in Narayan & Yi (1995). On the one hand, this implies that the effective molecular weight for ions is $\mu_{\rm i} = 1.23$ and for electrons $\mu_{\rm e} = 1.14$, and on the other hand it defines the electron and ion number densities, $n_{\rm e}$ and $n_{\rm i}$, with respect to the energy density. In the following, we provide general formulae in which the factor $n_{\rm i}$ is replaced by the sum over ion species,

$$\bar{n} = \sum Z_j^2 n_j, \tag{44}$$

where Z_j and n_j are respectively the charge and number density of the jth ion species.

3.2. Radiative processes

We have to complete the set of equations given in Sect. 3 by specifying the physical processes that are involved in the radiative cooling. We consider a two-temperature plasma cooled by synchrotron radiation, inverse Compton process, and bremsstrahlung emission. A very convenient and general description of these cooling processes was presented by Narayan & Yi (1995). We closely follow their approximations and procedures, and also use their formulae (correcting one typo). For the reader's convenience and completeness, we summarize these author's description here. Electron-positron pair creation and annihilation is neglected but as shown by Björnsson et al. (1996) and Kusunose & Mineshige (1996) this is justified in most cases of interest.

In the following subsections, we determine the emission and absorption coefficients inside the torus corresponding to bremsstrahlung, synchrotron radiation, and Compton processes. The emission coefficient respectively (resp.) absorption coefficient, j_ν (resp. α_ν), allows us to compute the increment (resp. decrement) of specific intensity I_ν when progressing through the emitting medium by a small distance $\mathrm{d}l$

$$\begin{aligned} \mathrm{d}I_\nu &= j_\nu \, \mathrm{d}l, \\ \mathrm{d}I_\nu &= -\alpha_\nu I_\nu \, \mathrm{d}l. \end{aligned} \tag{45}$$

The cgs unit of j_ν is $\mathrm{erg\,cm^{-3}\,s^{-1}\,ster^{-1}\,Hz^{-1}}$, while α_ν is expressed in $\mathrm{cm^{-1}}$.

3.2.1. Bremsstrahlung

The rate at which energy is lost due to bremsstrahlung, $f_{br}^- = dE_{br}/dt\, dV$, includes emission from both ion-electron and electron-electron collisions (Svensson 1982; Stepney & Guilbert 1983)

$$f_{br}^- = f_{ei}^- + f_{ee}^-. \tag{46}$$

The ion-electron bremsstrahlung cooling rate is given by

$$f_{ei}^- = n_e \bar{n} \sigma_T \alpha_f m_e c^3 F_{ei}(\theta_e), \tag{47}$$

where $\alpha_f = 1/137$ is the fine structure constant and the function $F_{ei}(\theta_e)$ has the approximate form in units of $[\mathrm{erg\, s^{-1} cm^{-3}}]$

$$
\begin{aligned}
F_{ei}(\theta_e) &= 4 \left(\frac{2\theta_e}{\pi^3} \right)^{1/2} \left(1 + 1.781\, \theta_e^{1.34} \right), & \theta_e < 1, \\
&= \frac{9\theta_e}{2\pi} \left[\ln(1.123\, \theta_e + 0.48) + 1.5 \right], & \theta_e > 1.
\end{aligned}
\tag{48}
$$

In the original formula quoted by Stepney & Guilbert (1983), there is a number 0.42 instead of 0.48 (see Narayan & Yi 1995).

For the electron-electron bremsstrahlung cooling rate, Svensson (1982) gives the following formula

$$f_{ee}^- = n_e^2 r_e^2 \alpha_f m_e c^3 F_{ee}(\theta_e), \tag{49}$$

where the function $F_{ee}(\theta_e)$ is given in units of $[\mathrm{erg\, s^{-1}\, cm^{-3}}]$ and has the approximate form

$$
\begin{aligned}
F_{ee}(\theta_e) &= \frac{20}{9\pi^{1/2}} \left(44 - 3\pi^2 \right) \theta_e^{3/2} \\
&\quad \times \left(1 + 1.1\,\theta_e + \theta_e^2 - 1.25\,\theta_e^{5/2} \right), & \theta_e < 1, \\
&= 24\,\theta_e \left[\ln(2\eta\,\theta_e) + 1.28 \right], & \theta_e > 1,
\end{aligned}
\tag{50}
$$

where $r_e = e^2/m_e c^2$ is the classical radius of electron and the Euler number $\eta = \exp(-\gamma_E) = 0.5616$ is given by the Euler-Mascheroni constant, γ_E. And again, we replace in the original formula 5/4 with 1.28 (see Narayan & Yi 1995).

With the bremsstrahlung cooling rate given above, one can express the bremsstrahlung emission coefficient as

$$j_\nu^{br} = f_{br}^- \frac{1}{4\pi} \frac{h}{k_B T_e} \exp\left(-\frac{h\nu}{k_B T_e} \right) \bar{G}, \tag{51}$$

where h is the Planck constant, the $1/4\pi$ factor assumes isotropic emission in the emitter's frame and $\bar{G}$ is the velocity-averaged Gaunt factor given by Rybicki & Lightman (1986)

$$
\begin{aligned}
\bar{G} &= \left(\frac{3}{\pi} \frac{k_B T_e}{h\nu} \right)^{1/2}, & \frac{k_B T_e}{h\nu} < 1, \\
&= \frac{\sqrt{3}}{\pi} \ln\left(\frac{4}{\gamma_E} \frac{k_B T_e}{h\nu} \right), & \frac{k_B T_e}{h\nu} > 1.
\end{aligned}
\tag{52}
$$

3.2.2. Synchrotron cooling

The emission coefficient for synchrotron emission by a relativistic Maxwellian distribution of electrons is given by (see Pacholczyk 1970)

$$j_\nu^{sy} = \frac{1}{4\pi} \frac{e^2}{c\sqrt{3}} \frac{4\pi n_e \nu}{K_2(1/\theta_e)} M(x_M), \tag{53}$$

with a factor $1/4\pi$ again for isotropic emission in the emitter's frame and the fitting function,

$$M(x_M) = \frac{4.0505\alpha}{x_M^{1/6}} \left(1 + \frac{0.40\beta}{x_M^{1/4}} + \frac{0.5316\gamma}{x_M^{1/2}} \right) \exp\left(-1.8899 x_M^{1/3} \right), \tag{54}$$

where

$$x_M = \frac{2\nu}{3\nu_0\,\theta_e^2}, \quad \nu_0 = \frac{eB}{2\pi m_e c} \tag{55}$$

and the parameters α, β, and γ are tabulated for a range of temperatures in Mahadevan et al. (1996). The fitting formula is valid only for $\theta_e \gtrsim 1$, i.e. $T_e \gtrsim 6 \times 10^9$ K, which is satisfied for applications to ion tori because the synchrotron emission that dominates the central regions of a torus comes, as in other advective flows, from relativistic electrons in the tail of the Maxwellian distribution. At lower temperatures or in the outer torus regions, the emission is dominated by bremsstrahlung. Below a critical frequency, ν_c, the synchrotron spectrum becomes self-absorbed. As the flow in ion tori is very much akin to a spherical flow, this frequency can be obtained by equating the synchrotron emission in a sphere of some radius, R [cm], to the Rayleigh-Jeans blackbody emission from the surface of that sphere and solving for x_M, which is then substituted into

$$\nu_c = \frac{3}{2}\nu_0\,\theta_e^2 x_M. \tag{56}$$

We assume that at low frequencies, $\nu < \nu_c$, the absorption is locally given by Kirchhoff's law, i.e., the low-frequency part of the synchrotron emission behaves like a blackbody.

3.2.3. Compton cooling

The soft bremsstrahlung and synchrotron photons in an ion torus filled with a thermal distribution of electrons are (inverse) Compton scattered to higher energies. In the central regions of the flow in particular, this can be an important cooling mechanism. There is a probability $\mathcal{P}$ that a seed photon of some initial energy, $E_{in} = h\nu$, is in optically thin material scattered to an amplified energy $E_{out} = \mathcal{A} E_{in}$, where

$$\mathcal{P} = 1 - \exp\left(-\tau_{es} \right), \quad \text{and} \quad \mathcal{A} = 1 + 4\theta_e + 16\theta_e^2. \tag{57}$$

Thus, the energy exchange between electrons and photons depends only on the electron temperature θ_e and the probability that a photon will interact with an electron, which is given by the electron scattering optical depth $\tau_{es} = \int n_e\, \sigma_T\, dl$. Dermer et al. (1991) and Esin et al. (1996) derived an approximate prescription for the energy enhancement factor due to Compton scattering, which is defined as the average energy change of a seed photon

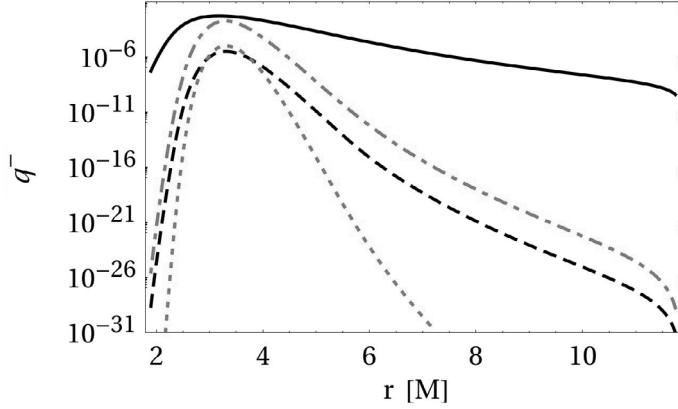$$\eta = 1 + \eta_1 + \eta_2 \left(\frac{x}{\theta_e} \right)^{\eta_3}, \tag{58}$$

where

$$
\begin{aligned}
\eta_1 &= \frac{\mathcal{P}(\mathcal{A} - 1)}{1 - \mathcal{P}\mathcal{A}}, \\
\eta_2 &= 3^{-\eta_3}\eta_1, \\
\eta_3 &= -1 - \ln\mathcal{P}/\ln\mathcal{A}.
\end{aligned}
\tag{59}
$$

The dimensionless energy is given by $x = \frac{h\nu}{m_e c^2}$. As the emerging photons cannot gain more energy than the electrons they collide

Fig. 3. Radiative cooling rates of a $\lambda = 0.7$ torus around a spin $a = 0.9M$ black hole. The contributions from bremsstrahlung (black, dashed), synchrotron (black, solid), Comptonised bremsstrahlung (grey, dot-dashed), and Comptonised synchrotron emission (grey, dotted) are shown as a function of radius.

with have, there is an upper limit to the energy gained, $x \lesssim 3\,\theta_e$. We note that in our simple ion torus scenario we apply, without loss of generality, the Thomson cross-section rather than the Klein-Nishina cross-section.

Comptonised emission is $\eta - 1$ times the seed photon distribution. The part of the spectrum that can be Comptonised lies between the critical synchrotron self-absorption edge, $x = x_c = h\nu_c/m_e c^2$, and $x = 3\,\theta_e$.

Comptonisation of bremsstrahlung emission is then given by

$$j_\nu^{\mathrm{br,C}} = j_\nu^{\mathrm{br}}\, 3\eta_1\, \theta_e \left\{ \left(\frac{1}{3} - \frac{x_c}{3\theta_e} \right) - \frac{1}{\eta_3 + 1} \left[\left(\frac{1}{3} \right)^{\eta_3+1} - \left(\frac{x_c}{3\theta_e} \right)^{\eta_3+1} \right] \right\}.$$
(60)

We note that the corresponding expression in Narayan & Yi (1995) has a typo that we have corrected here.

Comptonisation of synchrotron radiation that is emitted mostly at the self-absorption frequency, ν_c, is given by

$$j_\nu^{\mathrm{sy,C}} = j_\nu^{\mathrm{sy}} \left[\eta_1 - \eta_2\, (x_c/\theta_e)^{\eta_3} \right].$$
(61)

We calculate Comptonisation to second order and assume that photons that are up-scattered to θ_e form a Wien tail.

3.2.4. Total cooling

The total emission coefficient is the sum of all radiative contributions

$$j_\nu = j_\nu^{\mathrm{br}} + j_\nu^{\mathrm{br,C}} + j_\nu^{\mathrm{sy}} + j_\nu^{\mathrm{sy,C}}.$$
(62)

For a medium in local thermodynamic equilibrium (LTE) at temperature T, the emission coefficient given in Eq. (62) and the absorption coefficient are related by means of Kirchhoff's law

$$\alpha_\nu = \frac{j_\nu}{B_\nu(T)},$$
(63)

where B_ν is Planck's law of blackbody radiation. For the typical optical depth of ion tori, α_ν is negligible, thus the absorption can be safely ignored.

Integration of j_ν over the whole frequency range gives the total cooling rate q^- at each point (r, θ) in the torus. Figure 3 shows the different contributions to the total cooling rate from the equatorial plane, $\theta = \pi/2$, of a $\lambda = 0.3$ torus.

Table 1. Parameters for our reference ion torus.

Parameter	Value
a	$0.5M$
λ	0.3
β	0.1
n	3/2
ϵ_c [g cm^{-3}]	10^{-17}
ξ	0.1
$T_{e,c}$	$0.02\,T_{\mathrm{vir}}$
$i\,[\,^\circ]$	80

Notes. Parameter i is the inclination angle of the black hole rotational axis towards the line of sight. T_{vir} is the virial temperature.

Radiation that originates close to a black hole is influenced by various relativistic effects, such as the gravitational bending of light rays, gravitational redshift, and Doppler beaming. We ray-trace the emission derived in Eq. (62) from each point (r, θ) inside the Roche lobe equipotential back to the observer explicitly including all relativistic effects in light propagation. This is described in the next two sections.

4. Ray-tracing

We use the General relativitY Orbit Tracer of the Observatory of Paris[2] (GYOTO), presented in Vincent et al. (2011), which permits the integration of null and timelike geodesics in any analytical or numerical metric. It is optimised to compute geodesics in the Kerr spacetime efficiently, and is able to integrate the radiative transfer equation in optically thin media.

The required inputs for GYOTO are the values of the emission coefficient, j_ν, and absorption coefficient, α_ν, at any point within the torus. These quantities, defined in Sect. 3.2, are known analytically for the ion torus, so the integration is straightforward. In particular, the absorption coefficient is zero everywhere.

Photons are launched from the observer's screen, which is assumed to be spatially at rest at $r = 100\,M$, in a given specified solid angle. The null geodesics are integrated until the torus is reached (or until the photon escapes too far from the torus) and the specific intensity I_ν is updated at each step inside the torus by using Eq. (45). A map of specific intensity is thus obtained for a given set of directions on sky. It is then straightforward to compute the observed specific flux F_ν by summing these values of specific intensities over all directions of incidence.
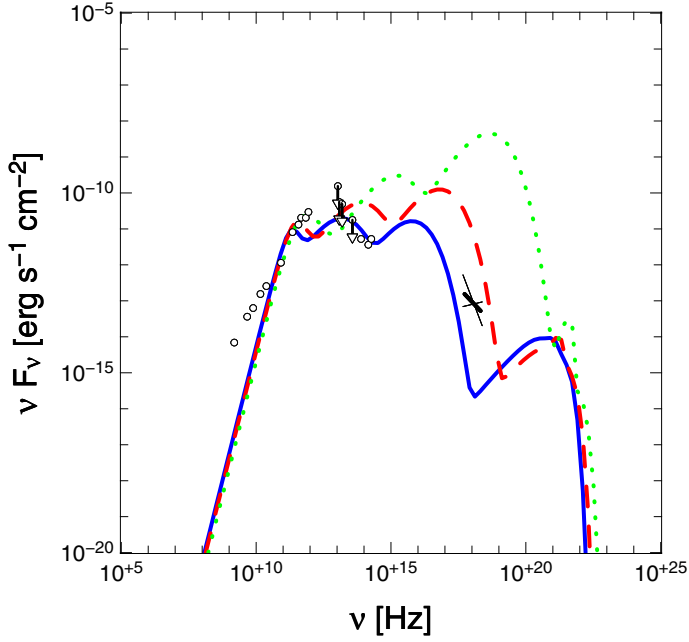
Two kinds of GYOTO-computed quantities are presented below. The spectra (Figs. 4–9) show the quantity $\nu\,F_\nu$ for different values of frequencies. The images (Fig. 10) are maps of specific intensity I_ν.

We stress that the whole C++ code for the ion torus is now included in the open source GYOTO code, which is available at the above-mentioned URL.
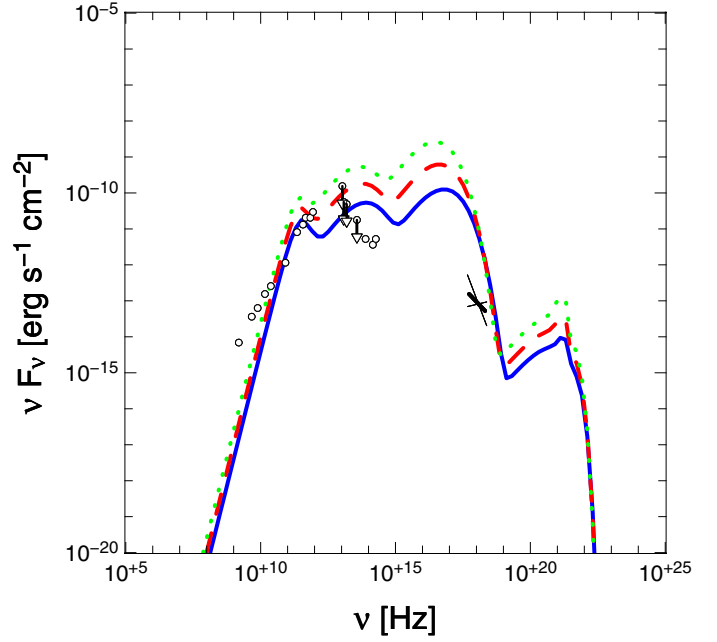
5. The spectra and images of ion tori

This section presents the spectra and images of an ion torus surrounding a Kerr black hole. Table 1 gives the reference values of the parameters used for the computations. The value chosen for the central density ϵ_c is standard for Sgr A* (see e.g. the values in Yuan et al. 2003; Liu et al. 2004; Mościbrodzka et al. 2009; Dodds-Eden et al. 2010). Various parameters are varied in the
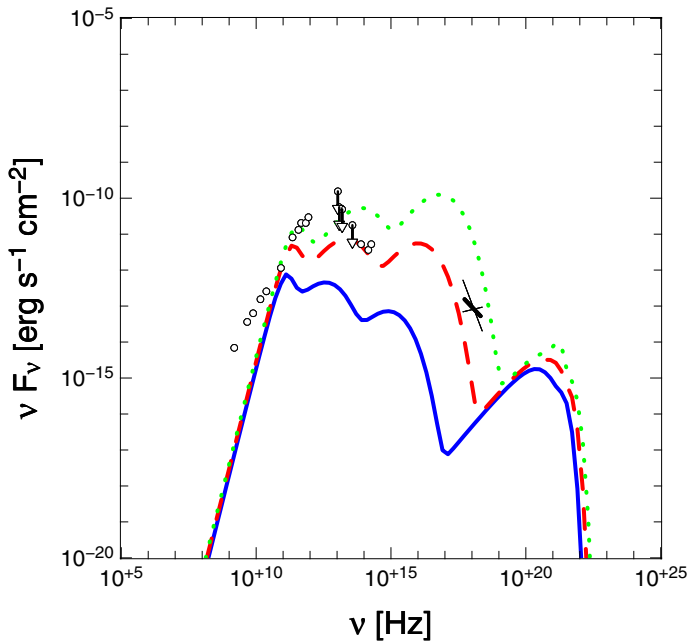
---

[2] Freely available at the URL `http://gyoto.obspm.fr`

Fig. 4. Impact of spin on an ion torus spectrum: $a = 0$ (solid blue), $0.5M$ (dashed red), or $0.9M$ (dotted green). All other parameters are set to their reference values listed in Table 1. The black observed data are taken from Zhao et al. (2001), Zylka et al. (1995), Marrone et al. (2008) for radio and sub-mm data, Telesco et al. (1996), Cotera et al. (1999), Eckart et al. (2006), Schödel et al. (2007) for far- and mid-infrared data, Genzel et al. (2003) for near-infrared data, and Baganoff et al. (2003) for the X-ray bow tie. The downward pointing arrows refer to upper values. Note that we do not present the fitted spectra here.
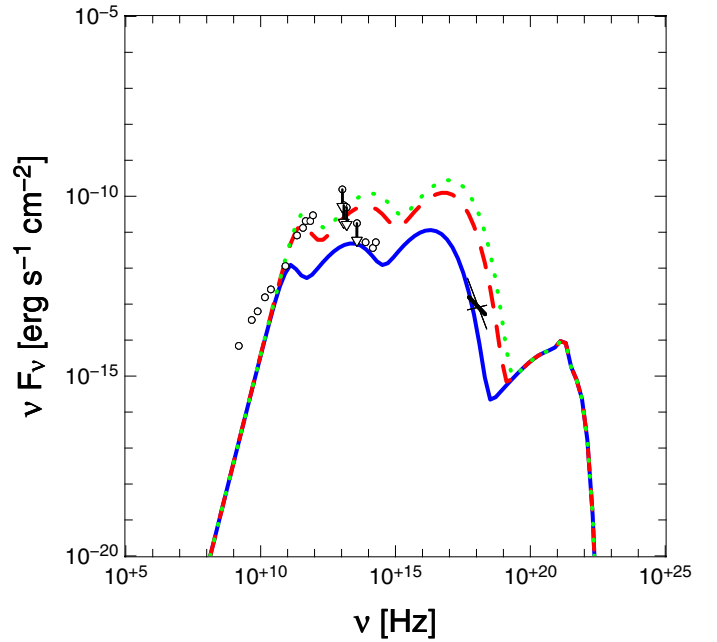

Fig. 5. Impact of central temperature: $T_0/T_{vir} = 0.01$ (solid blue), 0.015 (dashed red), or 0.02 (dotted green).

computations: the spin, a, the dimensionless angular momentum, λ, the magnetic to total pressure ratio, β, the electron to ion temperature ratio, ξ, the ratio of the central electron temperature to the virial temperature, and the inclination, i.

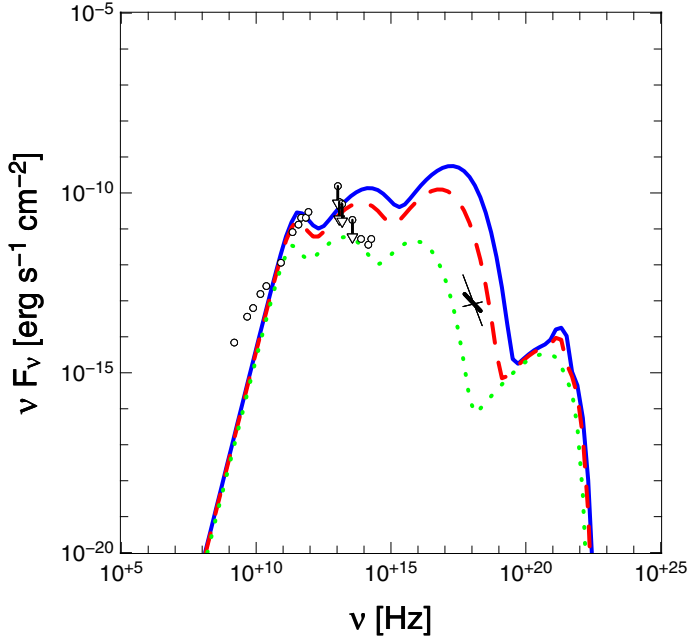Sections 5.1 and 5.2 describe the impact of these parameters on the spectrum and image of the ion torus.

Fig. 6. Impact of angular momentum: $\lambda = 0.3$ (solid blue), 0.45 (dashed red), or 0.6 (dotted green).

Fig. 7. Impact of pressure ratio: $\beta = 0.01$ (solid blue), 0.1 (dashed red), or 0.2 (dotted green).
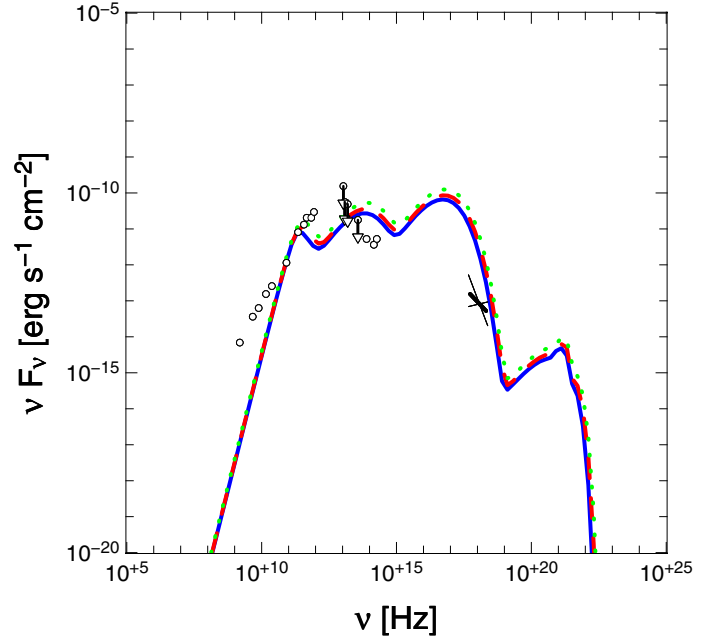
5.1. Torus spectra

Figures 4 to 9 show the impact of various parameters on the observed spectrum of an ion torus. All parameters that have not explicitly specified values are set according to Table 1. These figures show that the ion torus model is able to account for the general features of the observed data, by appropriately tuning the various parameters. This includes the X-ray flare "bow tie" which in the ion torus model may originate from soft photons that are inverse Compton scattered by the same population of hot electrons that is responsible for the synchrotron emission. Only the flattening of the spectrum at low frequencies is never matched, which is due to the absence of a non-thermal electron

Fig. 8. Impact of temperature ratio: $\xi = 0.08$ (solid blue), 0.1 (dashed red), or 0.2 (dotted green).

Fig. 9. Impact of inclination: $i = 40°$ (solid blue), 60° (dashed red), or 80° (dotted green).

distribution in our model, as first pointed out by Mahadevan (1998) and demonstrated by Özel et al. (2000) and Yuan et al. (2003). A more evolved model taking into account this effect will thus be developed in future work.

Figure 4 shows that varying the spin significantly alters the emission. This is because at high black hole spins the accretion torus shrinks and moves very close to the black hole. Therefore, the flux is shifted to slightly higher energies. Increasing the spin enhances the synchrotron flux, but softens bremsstrahlung.

Figure 5 shows that increasing the central temperature implies that there is a displacement of the whole spectrum towards higher fluxes. The same effect is obtained by increasing the dimensionless angular momentum λ (Fig. 6). This is because the torus puffs up like a balloon as λ increases (see Fig. 1), thus providing more flux.

Figures 7 and 8 show that increasing either the pressure ratio β or temperature ratio ξ has an opposite impact: a higher β leads to higher synchrotron flux, while a higher ξ gives a smaller flux. This is because increasing β increases the magnetic field strength, while increasing ξ decreases $\boldsymbol{B}$ (see Eq. (41)).

Figure 9 shows that the inclination has little effect on the spectrum. Although the number of illuminated pixels is smaller at higher inclination, the beaming effect is more important. These two phenomena have opposite effects, and the resulting spectrum does not change much.

Future work will be devoted to constraining the various parameters, in particular Sgr A*'s spin, by fitting these spectra to observed data.

5.2. Torus images

Each image is a superimposition of a first-order image (the thick distorted ring) and higher-order images (the circles centred on the black hole) produced by photons that swirl around the black hole before reaching the observer. There is also a very fine circle of light in each image, that consists of photons originating from a location just outside the photon orbit (see e.g. Bardeen et al. 1972, for a definition). Photons that escape from the region
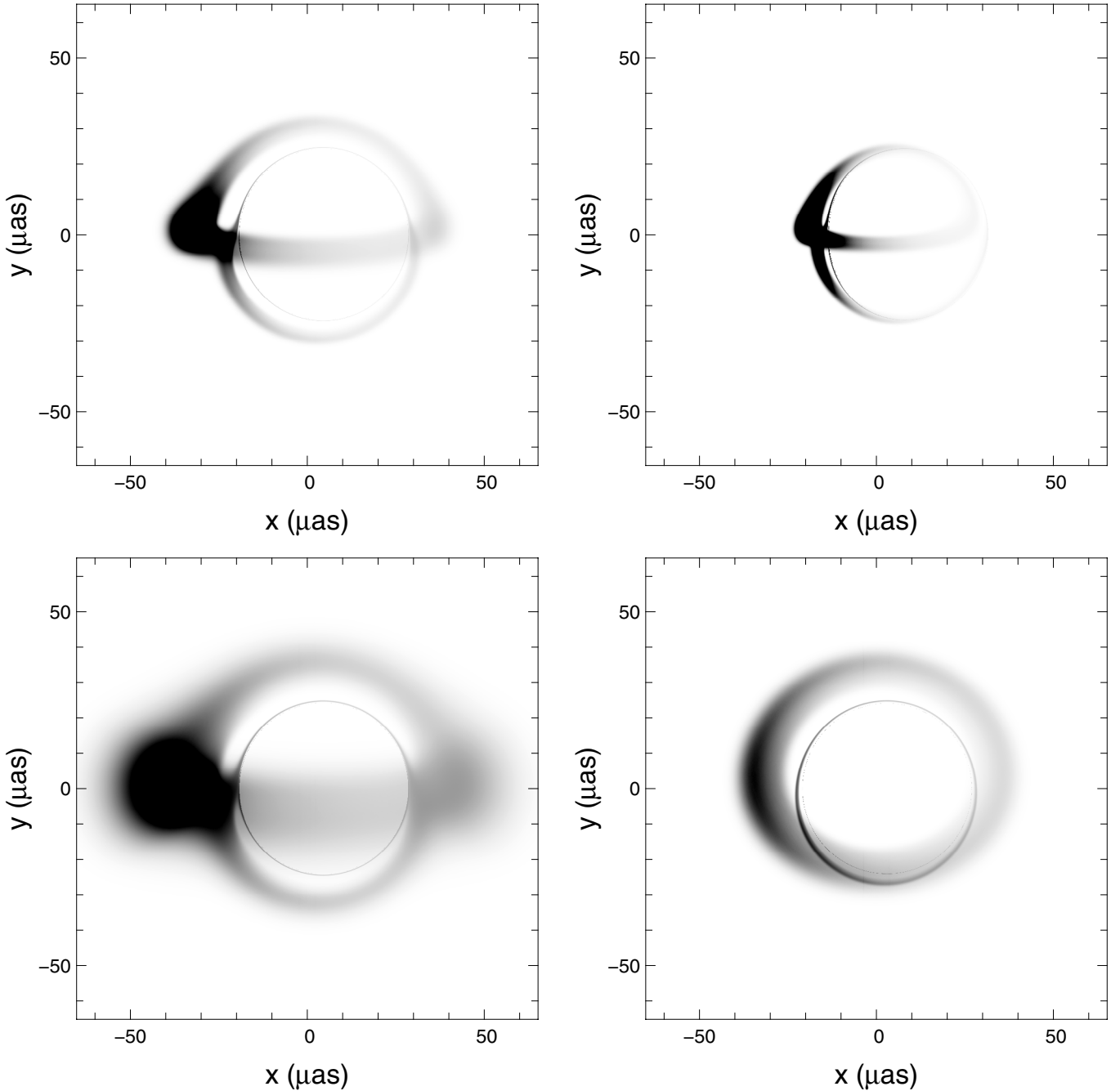
inside the photon orbit are so severely red-shifted that they create an area of reduced intensity on the observer's screen: this is the so-called "black hole silhouette" (which is also known as the black hole shadow; Falcke et al. 2000).

Our interest in these images is the following. Knowing the particular extent and shape of the accreting region from observations allows us to constrain various parameters of the flow. In particular, the location and shape of the photon orbit contains information on the geometry of spacetime. Increasing spin displaces the thin photon ring in the image plane off centre and $a \gtrsim 0.9M$ introduces in addition distortion. Black hole spin, torus dimensionless angular momentum and inclination have each a huge and characteristic impact on the observed image of the torus as depicted in Fig. 10. This is also revealed in the spectra Figs. 4 and 6. The inclination angle, however, does not influence the spectra in a commensurate way (Fig. 9).

The required technique of measurement of the black hole silhouette is already available thanks to recent progress in millimetre Very Long Baseline Interferometry (mm-VLBI) (see Doeleman et al. 2008). With the near-future sub-mm VLBI instruments direct observation of processes in the range between 5–40 Schwarzschild radii will become feasible and with it also the potential to image radiation from an accretion structure and, possibly, to deduce the existence of an event horizon.

6. Conclusions and perspectives

We have calculated electromagnetic spectra and images of accretion structures around the central black hole in Sgr A* using a simple analytic model of "ion tori" very similar to these described in the well-known paper by Rees et al. (1982). Our results depend on observationally unknown tunable parameters of the model, particularly the black hole spin. The hope is that fitting these analytic models to observations could *practically* restrict the allowed parameter range, so that future sophisticated MHD simulations of Sgr A* (which are similar to the more advanced ones of Dibi et al. 2012) will be more tightly constrained.

Fig. 10. *Upper left:* image of the reference ion torus corresponding to the parameters listed in Table 1, as observed by an observer on Earth, in inverted colours (the darker, the more luminous). The display is intentionally saturated for a better rendering of the less luminous parts of the image. *Upper right:* same as in the upper left but with the spin parameter increased to $a = 0.9M$. *Lower left:* same as in the upper left but with dimensionless angular momentum increased to $\lambda = 0.6$. *Lower right:* same as in the upper left but with the inclination angle decreased to $i = 40°$.

One interesting question here is how accurate the simple analytic models are compared with advanced MHD simulations. We are working on a comparison of our spectra and images with these calculated by Dibi et al. (2012). If the preliminary impression that these images and spectra are indeed *very* similar were to be confirmed by the test, then it would be much easier to fit theory to observations, and in particular to eventually *measure* the black hole spin in Sgr A*.

We plan to expand our models of ion tori to include a more complete coverage of the parameter space in connection with a "general" angular momentum distribution (as in Qian et al. 2009) and to include, directly and analytically, large-scale magnetic fields (as in Komissarov 2006). We also plan to calculate models of ion tori in a non-Kerr background (as advocated by Psaltis and collaborators, e.g., Psaltis et al. 2008; Johannsen & Psaltis 2010) to possibly constrain gravity in the strong-field regime of alternative gravity theories to Einstein's general relativity. In the context of flares it may also be interesting to examine non-stationary ion tori (as in Abramowicz et al. 1983).

References

Abramowicz, M., Jaroszynski, M., & Sikora, M. 1978, A&A, 63, 221

Abramowicz, M. A., Henderson, P. F., & Ghosh, P. 1983, MNRAS, 203, 323

Abramowicz, M. A., Chen, X., Kato, S., Lasota, J.-P., & Regev, O. 1995, ApJ, 438, L37

Baganoff, F. K., Maeda, Y., Morris, M., et al. 2003, ApJ, 591, 891

Bardeen, J. M., Press, W. H., & Teukolsky, S. A. 1972, ApJ, 178, 347

Björnsson, G., Abramowicz, M. A., Chen, X., & Lasota, J. 1996, ApJ, 467, 99

Blaes, O. M. 1987, MNRAS, 227, 975

Bower, G. C., Falcke, H., Herrnstein, R. M., et al. 2004, Science, 304, 704

Broderick, A. E., Loeb, A., & Reid, M. J. 2011, ApJ, 735, 57

Cotera, A., Morris, M., Ghez, A. M., et al. 1999, in The Central Parsecs of the Galaxy, ed. H. Falcke, A. Cotera, W. J. Duschl, F. Melia, & M. J. Rieke, ASP Conf. Ser., 186, 240

Dermer, C. D., Liang, E. P., & Canfield, E. 1991, ApJ, 369, 410

Dexter, J., Agol, E., Fragile, P. C., & McKinney, J. C. 2010, ApJ, 717, 1092

Dibi, S., Drappeau, S., Fragile, P. C., Markoff, S., & Dexter, J. 2012 [arXiv:1206.3976]

Dodds-Eden, K., Sharma, P., Quataert, E., et al. 2010, ApJ, 725, 450

Doeleman, S. S., Weintroub, J., Rogers, A. E. E., et al. 2008, Nature, 455, 78

Eckart, A., Schödel, R., Meyer, L., et al. 2006, A&A, 455, 1

Eisenhauer, F., Perrin, G., Brandner, W., et al. 2008, SPIE Conf. Ser., 7013, 70132A

Eisner, J. A., Akeson, R., Colavita, M., et al. 2010, SPIE Conf. Ser., 7734, 773411

Esin, A. A., Narayan, R., Ostriker, E., & Yi, I. 1996, ApJ, 465, 312

Esin, A. A., McClintock, J. E., & Narayan, R. 1997, ApJ, 489, 865

Falcke, H., Melia, F., & Agol, E. 2000, ApJ, 528, L13

Genzel, R., Schödel, R., Ott, T., et al. 2003, Nature, 425, 934

Gillessen, S., Eisenhauer, F., Trippe, S., et al. 2009, ApJ, 692, 1075

Goldston, J. E., Quataert, E., & Igumenshchev, I. V. 2005, ApJ, 621, 785

Hilburn, G., Liang, E., Liu, S., & Li, H. 2010, MNRAS, 401, 1620

Huang, L., Cai, M., Shen, Z., & Yuan, F. 2007, MNRAS, 379, 833

Ichimaru, S. 1977, ApJ, 214, 840

Jaroszynski, M., Abramowicz, M. A., & Paczynski, B. 1980, Acta Astron., 30, 1

Johannsen, T., & Psaltis, D. 2010, ApJ, 718, 446

Komissarov, S. S. 2006, MNRAS, 368, 993

Kusunose, M., & Mineshige, S. 1996, ApJ, 468, 330

Liu, S., Petrosian, V., & Melia, F. 2004, ApJ, 611, L101

Mahadevan, R. 1998, Nature, 394, 651

Mahadevan, R., Narayan, R., & Yi, I. 1996, ApJ, 465, 327

Marrone, D. P., Baganoff, F. K., Morris, M. R., et al. 2008, ApJ, 682, 373

Mościbrodzka, M., Gammie, C. F., Dolence, J. C., Shiokawa, H., & Leung, P. K. 2009, ApJ, 706, 497

Narayan, R., & Popham, R. 1993, Nature, 362, 820

Narayan, R., & Yi, I. 1994, ApJ, 428, L13

Narayan, R., & Yi, I. 1995, ApJ, 452, 710

Narayan, R., Yi, I., & Mahadevan, R. 1995, Nature, 374, 623

Özel, F., Psaltis, D., & Narayan, R. 2000, ApJ, 541, 234

Pacholczyk, A. G. 1970, Radio astrophysics. Nonthermal processes in galactic and extragalactic sources (San Francisco: Freeman)

Papaloizou, J. C. B., & Pringle, J. E. 1984, MNRAS, 208, 721

Paumard, T., Perrin, G., Eckart, A., et al. 2008, in The Power of Optical/ IR Interferometry: Recent Scientific Results and 2nd Generation, ed. A. Richichi, F. Delplancke, F. Paresce, & A. Chelli, 313

Psaltis, D., Perrodin, D., Dienes, K. R., & Mocioiu, I. 2008, Phys. Rev. Lett., 100, 119902

Qian, L., Abramowicz, M. A., Fragile, P. C., et al. 2009, A&A, 498, 471

Rees, M. J., Begelman, M. C., Blandford, R. D., & Phinney, E. S. 1982, Nature, 295, 17

Rybicki, G. B., & Lightman, A. P. 1986, Radiative Processes in Astrophysics (Wiley-VCH)

Schödel, R., Ott, T., Genzel, R., et al. 2002, Nature, 419, 694

Schödel, R., Eckart, A., Mužić, K., et al. 2007, A&A, 462, L1

Shapiro, S. L., Lightman, A. P., & Eardley, D. M. 1976, ApJ, 204, 187

Shcherbakov, R. V., Penna, R. F., & McKinney, J. C. 2012, ApJ, accepted [arXiv:1007.4832]

Stepney, S., & Guilbert, P. W. 1983, MNRAS, 204, 1269

Svensson, R. 1982, ApJ, 258, 335

Telesco, C. M., Davidson, J. A., & Werner, M. W. 1996, ApJ, 456, 541

Vincent, F. H., Paumard, T., Gourgoulhon, E., & Perrin, G. 2011, Class. Quant. Grav., 28, 225011

Yuan, F., Quataert, E., & Narayan, R. 2003, ApJ, 598, 301

Zhao, J.-H., Bower, G. C., & Goss, W. M. 2001, ApJ, 547, L29

Zylka, R., Mezger, P. G., Ward-Thompson, D., Duschl, W. J., & Lesch, H. 1995, A&A, 297, 83